Progress in Propulsion Physics **4** (2013) 539-568
DOI: 10.1051/eucass/201304539

EXTENDED LES-PaSR MODEL FOR SIMULATION OF TURBULENT COMBUSTION

V. Sabelnikov[1] **and C. Fureby**[2]

[1]ONERA — The French Aerospace Lab
Palaiseau 91761, France

[2]Defense Security Systems Technology
The Swedish Defense Research Agency — FOI
Tumba Stockholm 14725, Sweden

In this work, a novel model for Large Eddy Simulations (LES) of high Reynolds moderate Damköhler number turbulent flames is proposed. The development is motivated by the need for more accurate and versatile LES combustion models for engineering applications such as jet engines. The model is based on the finite rate chemistry approach in which the filtered species equations of a reduced reaction mechanism are solved prior to closure modeling. The modeling of the filtered reaction rate provides the challenge: as most of the chemical activity, and thus also most of the exothermicity occurs on the subgrid scales, this model needs to be based on the properties of fine-scale turbulence and mixing and Arrhenius chemistry. The model developed here makes use of the similarities with the mathematical treatment of multiphase flows together with the knowledge of fine-scale turbulence and chemistry obtained by Direct Numerical Simulation (DNS) and experiments. In the model developed, equations are proposed for the fine-structure composition and volume fraction that are solved together with the LES equations for the resolved scales. If subgrid convection can be neglected, the proposed model simplifies to the Partially Stirred Reactor (PaSR) model. To validate the proposed LES model, comparisons with experimental data and other LES results are made, using other turbulence chemistry interaction models, for a lean premixed bluff-body stabilized flame.

1 INTRODUCTION

Predictive modeling of turbulent combustion is becoming increasingly important for the development of air-, land-, and marine gas turbines, air-breathing engines, internal combustion (IC) engines, and for studies of, e. g., ammunition and waste destruction as well as fire spread. Reynolds Averaged Navier–Stokes

(RANS) based combustion models [1] have been successful in predicting some gross features of combustion such as combustor exit temperatures, whereas they are unable to predict transient phenomena such as combustion instabilities, cycle-to-cycle variations, self-ignition, and emission formation.

Large eddy simulation based combustion models [2, 3] is a promising alternative [4–6] that can provide accurate data for improvement of combustion devices. The idea of LES is to compute the large (energetic) scales of the flow, affected by the boundary conditions, whilst modeling the small (less energetic) scales of the flow. For nonreactive flows, this translates into providing closure models for the subgrid transport terms [2, 4], whilst for reacting flows also the filtered mixing and (highly nonlinear) reaction rate terms require closure modeling [4–6] as the reaction zone is not often well resolved on the grid.

To overcome these difficulties, several methods have been developed, such as:

(1) *Flamelet Progress Variable* (LES-FPV) *models*, including G-equation [7] and flame surface density [8, 9] models in which the reactions are assumed to take place in thin layers, separating the reactant mixture from the product mixture, wrinkled by the turbulence;

(2) *Probability Density Function models* (LES-PDF) [10] employing presumed shape or transported probability density functions to model the filtered reaction rates;

(3) *Finite Rate Chemistry models* (LES-FRC) including the Thickened Flame Model (LES-TFM) [11], LES-PaSR model [12] as well as the Eddy Dissipation Concept (LES-EDC) model [13] using different mathematical and phenomenological models of the filtered reaction rates;

(4) *Conditional Moment Closure* (LES-CMC) models [14] in which the species equations are conditionally averaged on a few variables on which the reaction rates are critically known to depend; and

(5) *Linear Eddy Models* (LES-LEM) [15] using a grid-within-the-grid approach to solve one-dimensional (1D) species equations with full resolution.

All these models have certain features that limit their usefulness, in particular, for engineering applications, in different ways, and therefore, it is desirable to develop more versatile and cost-effective LES combustion models. The commonly applied class of LES-FPV models, based on propagating fronts, with diffusion and chemistry as the principal physical mechanisms, are not well adapted to situations where convection and chemistry dominate, as in some industrial combustion applications and in supersonic combustion.

Here, a novel FRC-LES model for high Reynolds (Re) moderate Damköhler (Da) number turbulent combustion is proposed. The concept is based on the ideas of Chomiak [16, 17], later refined by Magnussen and Ertesvåg [13, 18],

which, in turn, are based on Batchelor and Townsend [19], suggesting that at high Re numbers, turbulent fine structure is not uniformly distributed but concentrated in small isolated regions, whose volume is a small fraction of the total volume. This has recently been verified by DNS in nonreactive [20] and reactive [21, 22] flows.

The core of the proposed model is the use of a multiphase analogy for modeling the high-intensity fine-scale structures embedded in low-intensity background turbulence. The model includes the PaSR model [12] as a limiting case when subgrid convection is neglected, and thus, the model will be referred to as the Extended PaSR (EPaSR) model. Here, the EPaSR model has been developed and tested against experimental data and other LES predictions, using the LES-FPV, TFM, EDC, and PaSR models, for a lean premixed bluff-body stabilized flame. The proposed LES-EPaSR model reproduces the experimental data well, and shows improved agreement over conventional model predictions. Although more expensive than the conventional models, the LES-EPaSR model is much cheaper than DNS and seems to be both accurate, computationally efficient, and robust.

2 A CONCEPTUAL REPRESENTATION OF HIGH REYNOLDS TURBULENT COMBUSTION

To develop successful physically-based subgrid Turbulence Chemistry Interaction (TCI) models for LES-FRC, one has to take into account that the spatiotemporal distribution of velocity gradients have a profound impact on the spatiotemporal topology of the chemical reaction regions in turbulent flows. As first noticed by Batchelor and Townsend [19], (in nonreactive flow) the velocity gradients are highly intermittent, which means that the fine structures, possessing most of the small-scale turbulence, are distributed nonuniformly, with the intermittency increasing with increasing Re number. Kuo and Corrsin [23] further suggest that the fine-structure regions consist of topological structures such as vortex sheets, ribbons, and tubes folded in specific regions of the flow. More recently, DNS (see, e. g., [20–22]) provided support to this view, revealing how high intensity vortices merge in complex shaped filaments that are embedded into sheets or arcs of low(er) intensity vorticity. This picture of the small-scale turbulence is dissimilar from the Kolmogorov turbulence theory (K41) [24, 25], in which the fine structures, and related quantities like dissipation, are distributed quasi-uniformly. The statistics of the fine structures in the K41 theory is determined only by the Kolmogorov length and time scales, $\ell_{\mathrm{K}} = \left(\nu^3/\varepsilon\right)^{1/4}$, and $\tau_{\mathrm{K}} = (\nu/\varepsilon)^{1/2}$, respectively [24, 25], in which ν denotes the molecular viscosity and ε the mean dissipation.

Kolmogorov [26] and Oboukhov [27] proposed in 1962 a modified theory of small-scale turbulence (the K62 theory) that incorporate also intermittency, following the remark of Landau and Lifshitz [28]. The most important result of this K62 theory is that the statistics of the fine structures is determined not just by ℓ_K and τ_K, as was supposed in the K41 theory, but also by the integral scales, ℓ_I and τ_I. This interrelation of the Kolmogov and larger scales can be illustrated by considering a slender region in a turbulent flow with dimensions ℓ_I and $\ell_K(\ll \ell_I)$. This slender region is thus subjected to the stretch produced by the velocity gradient of larger vortices, u'/ℓ_I where u' represents the fluctuating velocity. Since the velocity is correlated to a length of order ℓ_I, it may be assumed that the characteristic time scale of this stretch is of order ℓ_I/u', being applied over a length of order ℓ_I. This situation is similar to Burgers vortices, and the characteristic time of this slender region will be of the order of integral time scale ℓ_I/u'. For further details about intermittency in high Re turbulent flows refer to [29–33].

Recent DNS of combustion (at moderate Re and Da numbers) (see, e. g., [21, 22]) show a similar organization of the flow, with fine-structure vortices at the flame being essentially parallel to the flame whereas those behind the flame are mostly perpendicular to the flame. Figures 1*a* and 1*b* show the results in terms

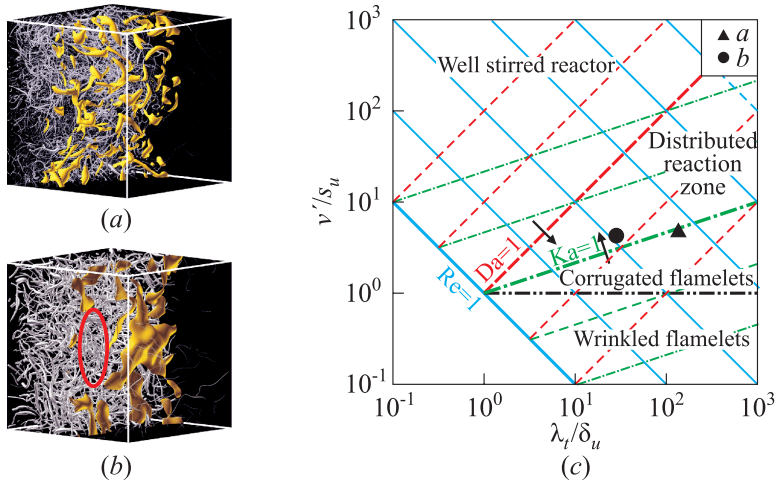

Figure 1 Results from recent DNS of combustion at moderate Re and Da numbers from [22]: (*a*) and (*b*) show isosurfaces of the heat release (yellow) and vorticity (grey) from a planar flame in homogeneous isotropic turbulence at Re ≈ 515, Da ≈ 21, and Ka = 1.3 (*a*) and Re = 141, Da ≈ 5, and Ka ≈ 2.8 (*b*). In (*c*), these DNS are shown by filled symbols in the Borghi diagram.

of vorticity and heat release structures from DNS of planar flame propagation in homogeneous istotropic turbulence from Tanahashi *et al.* [22]. The regions of high heat release and volumetric expansion are typically found to exist in tubular and sheet-like structures, distributed between the high and low intensity vortical regions bracketing the flame. The topology of the regions in which the chemical reactions and heat release occur are observed to correlate with filaments of vorticity, defining fine structure regions, and are found to be more tube-like and sparse for higher Karlowitz (Ka) number (Ka $=\mathrm{Re}^{1/2}\mathrm{Da}$ [1]). From a physical point of view, this observation is not surprising as the fine structures contain the molecular fluxes on which the mixing and chemical reactions are so heavily depending. The consequence of this observation is important for the formulation of TCI models. If the spectrum of life times of the fine structures can be allowed to vary from the Kolmogorov time scale to the integral time scale, the micromixing times that inevitably must enter any subgrid TCI model have also to respect this wide range of time scales.

The proposed model that will be described next is formulated upon the cartoon of turbulence chemistry interaction sketched here and in Fig. 1.

3 LARGE EDDY SIMULATION COMBUSTION MODELING USING A MULTIPHASE ANALOGY

The reactive flow equations are the balance equations of mass, momentum, and energy describing convection, diffusion, and chemical reactions [1, 4–6, 10]. In LES [2], all variables are decomposed into resolved and unresolved (subgrid) components by a spatial filter such that $f = \tilde{f} + f''$ where $\tilde{f} = \overline{\rho f}/\overline{\rho}$ is the Favre (or density) filtered variable. Filtering the reactive flow equations yields:

$$\left.\begin{aligned}
\partial_t\left(\overline{\rho}\right) + \nabla\cdot\left(\overline{\rho}\tilde{\mathbf{v}}\right) &= 0\,;\\
\partial_t\left(\overline{\rho}\tilde{Y}_i\right) + \nabla\cdot\left(\overline{\rho}\tilde{\mathbf{v}}\tilde{Y}_i\right) &= \nabla\cdot\left(\overline{\mathbf{j}}_i - \mathbf{b}_i\right) + \overline{\dot{w}}_i\,;\\
\partial_t\left(\overline{\rho}\tilde{\mathbf{v}}\right) + \nabla\cdot\left(\overline{\rho}\tilde{\mathbf{v}}\otimes\tilde{\mathbf{v}}\right) &= -\nabla\overline{p} + \nabla\cdot\left(\overline{\mathbf{S}} - \mathbf{B}\right)\,;\\
\partial_t\left(\overline{\rho}\tilde{h}_s\right) + \nabla\cdot\left(\overline{\rho}\tilde{\mathbf{v}}\tilde{h}_s\right) &= \overline{\mathbf{S}}\cdot\nabla\tilde{\mathbf{v}} + \partial_t\left(\overline{p}\right) + \nabla\overline{p}\cdot\tilde{\mathbf{v}} + \nabla\cdot\left(\overline{\mathbf{h}} - \mathbf{b}_h\right)\\
&\quad + \overline{\rho}\tilde{\sigma} - \sum_{i=1}^{N}\left(\overline{\dot{w}}_i h^{\theta}_{f,i}\right)\,.
\end{aligned}\right\} \tag{1}$$

Here, ρ is the density; $\mathbf{v}$ is the velocity; p is the pressure; $\mathbf{S}$ is the viscous stress tensor; $h_s = \sum_i Y_i \int_{T_0}^{T} C_{p,i}\,dT$ is the sensible enthalpy; T is the temperature; $\mathbf{h}$ is the heat flux vector; Y_i is the species mass fraction; $\dot{w}_i$ is the species reaction rate; $\mathbf{j}_i$ is the species mass flux; $h^{\theta}_{f,i}$ are the species formation enthalpies; and σ

is the radiative heat loss which will be neglected. Note that the subgrid pressure fluctuations and dissipation terms are neglected in Eqs. (1).

The subgrid flow physics is concealed in the subgrid stress tensor

$$\mathbf{B} = \overline{\rho}\left(\widetilde{\mathbf{v}\otimes\mathbf{v}} - \tilde{\mathbf{v}}\otimes\tilde{\mathbf{v}}\right)$$

and flux vectors

$$\mathbf{b}_i = \overline{\rho}\left(\widetilde{\mathbf{v}Y_i} - \tilde{\mathbf{v}}\tilde{Y}_i\right) \; ; \quad \mathbf{b}_h = \overline{\rho}\left(\widetilde{\mathbf{v}h} - \tilde{\mathbf{v}}\tilde{h}\right) \; ,$$

which results from filtering the convective terms. Following [6], one may postulate that the gas mixture behaves as a linear viscous fluid with Fourier heat conduction and Fickian species diffusion such that $\overline{\mathbf{j}}_i \approx D_i\nabla\tilde{Y}_i$, $\overline{p} \approx \overline{\rho}R\tilde{T}$, $\overline{\mathbf{S}} \approx 2\mu\tilde{\mathbf{D}}_D$, and $\overline{\mathbf{h}} \approx \kappa\nabla\tilde{T}$, respectively. Here, $D_i = \mu/\mathrm{Sc}_i$ is the species diffusivities; R is the composition dependent gas constant; μ is the viscosity; $\tilde{\mathbf{D}}_D = \left(\nabla\tilde{\mathbf{v}} + \nabla\tilde{\mathbf{v}}^{\mathrm{T}}\right)/2 - (\nabla\cdot\tilde{\mathbf{v}})\,\mathbf{I}/3$ is the deviatoric part of the rate of strain tensor; and $\kappa = \mu/\mathrm{Pr}$ is the thermal diffusivity where Sc_i and Pr are the Schmidt and Prandtl numbers, respectively. Finally, the filtered reactions rates are defined as

$$\overline{\dot{w}}_i = M_i \sum_{j=1}^{M} P_{ij}\overline{\hat{\dot{w}}}_j$$

where M_i is the molar mass of specie i; $P_{ij} = P''_{ij} - P'_{ij}$ are the stoichiometric coefficients; and

$$\hat{\dot{w}}_j = k_{fj}\prod_{k=1}^{N}\left(\frac{\rho Y_k}{M_k}\right)^{P'_{kj}} - k_{rj}\prod_{k=1}^{N}\left(\frac{\rho Y_k}{M_k}\right)^{P''_{kj}}$$

in which k_{fj} and k_{rj} being the Arrhenius forward and reverse rates of the jth reaction step, $k_{fj} = A_{fj}T^{\beta_j}\exp\left(-T_{a,j}/T\right)$, and β_j and $T_{a,j}$ the Arrhenius parameters.

3.1 Subgrid Flow Modeling

To close the LES equations (1), it is necessary to provide submodels for $\mathbf{B}$, $\mathbf{b}_i$, $\mathbf{b}_E$, and $\overline{\dot{w}_i}$, and considering first the subgrid stress tensor and flux vectors, these are not unique to reactive flows and therefore, closure models can be acquired from the plethora of subgrid models for nonreactive flows [2, 3]. Here, it is used the Mixed Model (MM) [34] with $\mathbf{B} = \overline{\rho}\left(\widetilde{\tilde{\mathbf{v}}\otimes\tilde{\mathbf{v}}} - \tilde{\tilde{\mathbf{v}}}\otimes\tilde{\tilde{\mathbf{v}}}\right) - 2\mu_k\tilde{\mathbf{D}}_D$, $\mathbf{b}_i = \overline{\rho}\left(\widetilde{\tilde{\mathbf{v}}\tilde{Y}_i} - \tilde{\tilde{\mathbf{v}}}\tilde{\tilde{Y}}_i\right) - \left(\mu_k/\mathrm{Sc}_t\right)\nabla\tilde{Y}_i$, and $\mathbf{b}_h = \overline{\rho}\left(\widetilde{\tilde{\mathbf{v}}\tilde{h}_s} - \tilde{\tilde{\mathbf{v}}}\tilde{\tilde{h}}_s\right) - \left(\mu_k/\mathrm{Pr}_t\right)\nabla\tilde{h}_s$ where the subgrid viscosity, $\mu_k = c_k\Delta k^{1/2}$, is provided by an equation for the subgrid kinetic energy k [34] and where Sc_t and Pr_t are the turbulent

Schmidt and Prandtl numbers. The model coefficients are calculated under the assumption of an infinite inertial subrange [2]. To reduce the computational cost, a *wall-modeled* LES was used, in which it is used a model [35] to handle the near-wall flow physics. This model is based on replacing the viscosity ($\mu + \mu_k$) and thermal and species diffusivities ($\mu/\mathrm{Pr} + \mu_k/\mathrm{Pr}_T$ and $\mu/\mathrm{Sc}_i + \mu_k/\mathrm{Sc}_T$, respectively) in the first grid point adjacent to the wall, with values consistent with those obtained from the well-known logarithmic law of the wall.

3.2 A Multiphase Framework for Subgrid Combustion Modeling

Considering next the filtered reaction rates $\overline{\dot{w}_i}$, incorporating the turbulence chemistry interactions, is notoriously difficult to model because of their nonlinear nature [1]. Using the phenomenological models [16, 17, 36], based on experimental data, and DNS results [20–22], included also in Fig. 1, a cartoon of turbulent mixing and combustion may be constructed. In this, turbulent reacting flows may be viewed as a muddle of vortex structures of different topological character, sheets, ribbons, and tubes, in which the tubes and ribbons carry most of the high-intensity vorticity and dissipation. This implies that the fine-structure regions, denoted by (*), are embedded in a surrounding fluid, here denoted by (^{0}), will be responsible for most of the molecular mixing, chemical reactions, and heat release. This cartoon is similar to that of [13, 18, 37] but here, a very different strategy based on an analogy with multiphase flow modeling will be employed for formulating the LES equations.

For the derivation of the proposed model, let henceforth $\psi = [Y_i, h_s]$ be the composition space, the evolution of which is governed by the local balance equation:

$$\partial_t (\rho\psi_i) + \nabla \cdot (\rho \mathbf{v} \psi_i) = \nabla \cdot \mathbf{k}_i + \dot{\omega}_i \tag{2}$$

where $\psi_i = Y_i$, $\mathbf{k}_i = \mathbf{j}_i$ and $\dot{\omega}_i = \dot{w}_i$ for $1 \leq i \leq N$, in which N denotes the number of species in the species equation (1_2) whereas $\psi_{N+1} = h_s$, $\mathbf{k}_{N+1} = \mathbf{h}$, and $\dot{\omega}_{N+1} = \mathbf{S} \cdot \nabla \mathbf{v} + \partial_t p + \nabla p \cdot \mathbf{v} - \sum_{i=1}^{N} \left(\overline{\dot{w}}_i h_{f,i}^{\theta} \right)$ are the terms in the energy equation (1_4). As for the theory of multiphase flows (see, e. g., [38]), a phase indicator function, I_α, with $\alpha = 1$ in the fine structures (*) and $\alpha = 0$ in the surroundings (^{0}), is next introduced to differentiate between these regions so that (2) becomes

$$\partial_t (\rho_\alpha \psi_{i,\alpha} I_\alpha) + \nabla \cdot (\rho_\alpha \psi_{i,\alpha} I_\alpha \mathbf{v}_\alpha) = \nabla \cdot (\mathbf{k}_{i,\alpha} I_\alpha) + \dot{\omega}_{i,\alpha} I_\alpha + M_{i,\alpha} \tag{3}$$

where $M_{i,\alpha}$ denote the exchange terms at the immaterial surface separating the fine structures and $\alpha = 0$ in the surroundings. By summing over α in (3),

provided that the exchange terms satisfy $\sum_{\alpha=0}^{1} (M_{i,\alpha}) = 0$, the composition space equations are recovered. In the framework of LES, the species mass fraction equations are filtered over space to obtain equations for the large energetic scales of motion. If one takes the filtering to correspond to a box-filter, covering the cell volume, ΔV, as often done in LES [2], the volume fraction of phase α is

$$\gamma_\alpha = \frac{1}{\Delta V} \int_{\Delta V} I_\alpha(\mathbf{x}, t)\, dV = \frac{\Delta V_\alpha}{\Delta V} = \overline{I}_\alpha \quad \text{with} \quad \sum_{\alpha=0}^{1} \gamma_\alpha = 1\,, \tag{4}$$

so that for products $I_\alpha \psi_{i,\alpha}$ and $\rho_\alpha \psi_{i,\alpha} I_\alpha$, it can easily be shown that $(\psi_{i,\alpha})_\alpha = \overline{\psi_{i,\alpha} I_\alpha}/\overline{I}_\alpha$ and $\overline{\rho_\alpha \psi_{i,\alpha} I_\alpha} = \gamma_\alpha \left(\overline{\rho_\alpha \psi_{i,\alpha}}\right)_\alpha = \gamma_\alpha (\overline{\rho}_\alpha)_\alpha \left(\tilde{\psi}_{i,\alpha}\right)_\alpha$. Filtering the local balance equations (2) then yields:

$$\partial_t \left(\gamma_\alpha (\overline{\rho}_\alpha)_\alpha \left(\tilde{\psi}_{i,\alpha}\right)_\alpha\right) + \nabla \cdot \left(\gamma_\alpha (\overline{\rho}_\alpha)_\alpha \left(\tilde{\psi}_{i,\alpha}\right)_\alpha (\tilde{\mathbf{v}})_\alpha\right) = \nabla \cdot \left(\gamma_\alpha \left(\overline{\mathbf{k}}_{i,\alpha}\right)_\alpha - \gamma_\alpha \mathbf{b}_i\right) + \gamma_\alpha \left(\overline{\dot{\omega}}_{i,\alpha}\right)_\alpha + \overline{M}_{i,\alpha}$$

where $\gamma_\alpha \mathbf{b}_i = \overline{\rho_\alpha \psi_{i,\alpha} I_\alpha \mathbf{v}} - \gamma_\alpha (\overline{\rho}_\alpha)_\alpha \left(\tilde{\psi}_{i,\alpha}\right)_\alpha (\tilde{\mathbf{v}})_\alpha$ denotes the subgrid transport term, which will typically be modeled by a conventional subgrid viscosity model. Summing over the filtered equations (4) results in that the filtered exchange terms satisfy $\sum_{\alpha=0}^{1} \left(\overline{M}_{i,\alpha}\right) = 0$, so that the LES composition space equations (1_2) and (1_4) are recovered. Returning next to the old notions, with $(^*)$ denoting the fine structures and $(^0)$ the surroundings, such that $\psi_i^* = \left(\tilde{\psi}_{i,1}\right)_1$ and $\psi_i^0 = \left(\tilde{\psi}_{i,2}\right)_2$ and $\tilde{\psi}_i = \gamma^* \psi_i^* + \gamma^0 \psi_i^0 = \gamma^* \psi_i^* + (1 - \gamma^*)\, \psi_i^0$, one then obtains the set of equations:

$$\left.\begin{aligned} \partial_t \left(\gamma^* \rho^* \psi_i^*\right) + \nabla \cdot \left(\gamma^* \rho^* \psi_i^* \mathbf{v}^*\right) &= \nabla \cdot \left(\gamma^* \left(\overline{\mathbf{k}}_i - \mathbf{b}_i\right)\right) + \gamma^* \overline{\dot{\omega}}_i^* + \overline{M}_i^*\,; \\ \partial_t \left(\gamma^0 \rho^0 \psi_i^0\right) + \nabla \cdot \left(\gamma^0 \rho^0 \psi_i^0 \mathbf{v}^0\right) &= \nabla \cdot \left(\gamma^0 \left(\overline{\mathbf{k}}_i - \mathbf{b}_i\right)\right) + \gamma^0 \overline{\dot{\omega}}_i^0 + \overline{M}_i^0\,. \end{aligned}\right\} \tag{5}$$

The above set of equations can be solved together for ψ_i^* and ψ_i^0 after which an LES quantity $\tilde{\psi}_i$ can be constructed from $\tilde{\psi}_i = \gamma^* \psi_i^* + (1 - \gamma^*)\, \psi_i^0$ once the fine structure volume fraction, γ^*, is known. A more convenient and straightforward approach is, however, to solve the balance equations for the fine-structure fractions ψ_i^* (5_1) together with the LES balance equations for $\tilde{\psi}_i$:

$$\left.\begin{aligned} \partial_t \left(\overline{\rho} \tilde{\psi}_i\right) + \nabla \cdot \left(\overline{\rho} \tilde{\mathbf{v}} \tilde{\psi}_i\right) &= \nabla \cdot \left(\overline{\mathbf{k}}_i - \mathbf{b}_i\right) + \overline{\dot{\omega}}_i\,; \\ \partial_t \left(\gamma^* \rho^* \psi_i^*\right) + \nabla \cdot \left(\gamma^* \rho^* \psi_i^* \mathbf{v}^*\right) &= \nabla \cdot \left(\gamma^* \left(\overline{\mathbf{k}}_i - \mathbf{b}_i\right)\right) + \gamma^* \overline{\dot{\omega}}_i^* + \overline{M}_i^*\,, \end{aligned}\right\} \tag{6}$$

once γ^* and $\overline{M}_i^*$ are provided and once the relation between $\overline{\dot{\omega}}_i$ and $\overline{\dot{\omega}}_i^*$ is established.

Based on the relationship between ψ_i^*, ψ_i^0, and $\tilde{\psi}_i$ and the nature of Eqs. (5) and (6), it becomes evident that $\overline{\dot{\omega}}_i = \gamma^* \overline{\dot{\omega}}_i^* + (1-\gamma^*)\,\overline{\dot{\omega}}_i^0$ and $\overline{M}_i^* + \overline{M}_i^0 = 0$. Most theoretical [16, 17], experimental (see, e. g., [35]), and computational (see, e. g., [21, 22]) observations suggest that most exothermal reactions mainly occur in the fine structures (see Fig. 1). This inevitably leads to the simplification that $\overline{\dot{w}}_i \approx \gamma^* \overline{\dot{w}}_i^*$ for all $i \leq N$, clearly emphasizing the importance of the volume fraction of the fine structures. In order to establish a link with probability density based models, the authors also note that

$$\overline{\dot{w}}_i = \int\limits_{\boldsymbol{\psi}} \wp(\boldsymbol{\psi}) \dot{w}_i(\boldsymbol{\psi})\, d\boldsymbol{\psi} = \gamma^* \overline{\dot{w}}_i^* + (1-\gamma^*)\,\overline{\dot{w}}_i^0 \approx \gamma^* \overline{\dot{w}}_i^* \quad \text{for all} \quad i \leq N$$

where $\wp(\boldsymbol{\psi}) = \gamma^* \delta\left(\boldsymbol{\psi} - \boldsymbol{\psi}^*\right) + (1-\gamma^*)\,\delta\left(\boldsymbol{\psi} - \boldsymbol{\psi}^0\right)$ is the probability density function. In addition, by summing over the N species equations in (5_1) and (5_2), taking explicitly into account that

$$\sum_{i=1}^{N} \left(\psi_i^*\right) = \sum_{i=1}^{N} \left(\psi_i^0\right) = 1\,; \quad \sum_{i=1}^{N} \left(\overline{\dot{\omega}}_i^*\right) = \sum_{i=1}^{N} \left(\overline{\dot{\omega}}_i^0\right) = 0\,,$$

it follows that

$$\left.\begin{aligned} \partial_t\left(\gamma^* \rho^*\right) + \nabla \cdot \left(\gamma^* \rho^* \mathbf{v}^*\right) &= \sum_{i=1}^{N} \left(\overline{M}_i^*\right)\,; \\ \partial_t\left(\gamma^0 \rho^0\right) + \nabla \cdot \left(\gamma^0 \rho^0 \mathbf{v}^0\right) &= \sum_{i=1}^{N} \left(\overline{M}_i^0\right) \end{aligned}\right\} \tag{7}$$

the sum of which must satisfy the continuity equation (1_1). This constraint subsequently results in that

$$\dot{m} = \sum_i \left(\overline{M}_i^*\right) = -\sum_i \left(\overline{M}_i^0\right)$$

where it is denoted by $\dot{m}$ the exchange rate of mass between the fine structures and the surroundings — responsible for subgrid mixing and reactions.

3.3 Subgrid Combustion Modeling

To provide a closure for $\dot{m}$, it was supposed that if there is a dynamic equilibrium state between the fine structures and the surroundings, which is characterized by the value γ_{eq}^* (which is to be discussed later), then mass exchange rate between the fine structures and the surroundings is zero, i. e., $\dot{m}(\gamma_{\text{eq}}^*) = 0$. For this

equilibrium state, the surface separating the surroundings and fine structures can be considered a material. Developing $\dot{m}$ in the vicinity of γ^*_{eq}, whilst retaining only the first-order linear term, assumed proportional to $(\gamma^* - \gamma^*_{\mathrm{eq}})$, results in that

$$\dot{m} = -\frac{\overline{\rho}\left(\gamma^* - \gamma^*_{\mathrm{eq}}\right)}{\tau^*} \tag{8}$$

where τ^* is the fine structure residence time and the term $\overline{\rho}/\tau^*$ follows from dimensional considerations. It should be noted that the hypothesis underlying (8) refers to high Re – moderate Da number flows, in which combustion takes place in concentrated regions, whose entire volume is a small fraction of the total volume. This situation is often observed in real combustion applications such as aero- and power generation gas turbines, ramjet and scramjet engines, jet engines, and large-scale furnaces. The application of this approach for lower Re numbers, in the flamelet regime, is not straightforward. From Eq. (8), it can be concluded that if $\dot{m} > 0$, $\gamma^* < \gamma^*_{\mathrm{eq}}$, the exchange rate of mass is directed from the surroundings to the fine structures. Otherwise, if $\dot{m} < 0$, $\gamma^* > \gamma^*_{\mathrm{eq}}$, then the exchange rate of mass is directed from the fine structures to the surroundings. Also, it can be noted that this exchange rate is due to convection through the interface separating fine structures and surroundings. Using Eq. (8), Eq. (7_1) becomes

$$\partial_t\left(\gamma^*\rho^*\right) + \nabla\cdot\left(\gamma^*\rho^*\tilde{\mathbf{v}}^*\right) = \dot{m} = -\frac{\overline{\rho}\left(\gamma^* - \gamma^*_{\mathrm{eq}}\right)}{\tau^*}\,. \tag{9}$$

Next, let consider the necessary modeling of the exchange terms $\overline{M}^*_i$ and $\overline{M}^0_i$ in Eq. (5). As follows from the core physical considerations, $\overline{M}^*_i$ and $\overline{M}^0_i$ contain two kinds of terms. The first type of term, here denoted by $\overline{\Theta}^*_i$ and $\overline{\Theta}^0_i$, is due to the exchange rate of mass between the fine structures and the surroundings (through the surface separating the fine structures and surroundings) as discussed above. If the exchange rate of mass is absent, as in the dynamic equilibrium state, the mass transport rate $\dot{m} = 0$, and these two terms become zero. The second type of term, here denoted by $\overline{\Omega}^*_i$ and $\overline{\Omega}^0_i$, is due to molecular diffusion through the interface between the fine structures and surroundings. Indeed, even if the exchange rate of mass is absent (i. e., dynamic equilibrium), there is exchange through the interface due to molecular diffusion. If $\psi^*_i = \psi^0_i$, these terms, however, turn to zero, as in this case there is no molecular diffusion. Based on the above considerations, the authors propose to model these exchange terms as

$$\left.\begin{aligned}
&\overline{M}^*_i = \overline{\Theta}^*_i + \overline{\Omega}^*_i\,; && \overline{M}^0_i = \overline{\Theta}^0_i + \overline{\Omega}^0_i\,;\\
&\overline{\Omega}^*_i = -\frac{\gamma^*\overline{\rho}\left(\psi^*_i - \psi^0_i\right)}{\tau^*}\,; && \overline{\Omega}^0_i = -\overline{\Omega}^*_i\,;\\
&\overline{\Theta}^*_i = \frac{1}{2}\left(\dot{m} + |\dot{m}|\right)\psi^0_i + \frac{1}{2}\left(\dot{m} - |\dot{m}|\right)\psi^*_i\,; && \overline{\Theta}^0_i = -\overline{\Theta}^*_i\,,
\end{aligned}\right\} \tag{10}$$

thereby satisfying $\sum_{\alpha=0}^{1}(M_{i,\alpha})=0$ (in fact, separately for both categories of terms, $\sum_{\alpha=0}^{1}(\Theta_{i,\alpha})=0$ and $\sum_{\alpha=0}^{1}(\Omega_{i,\alpha})=0$, as has to be). In correspondence with the underlying physics, it can be noted that if mass exchange is directed from the surroundings to the fine structures, $\dot{m}>0$, one find from Eqs. (10) that

$$\overline{\Theta}_i^* = \dot{m}\psi_i^0\,; \qquad \overline{\Theta}_i^0 = -\overline{\Theta}_i^* = -\dot{m}\psi_i^0\,.$$

Similarly, if the mass exchange is directed from the fine structures to the surroundings, i. e., for $\dot{m}<0$, one has:

$$\overline{\Theta}_i^* = \dot{m}\psi_i^*\,; \qquad \overline{\Theta}_i^0 = -\overline{\Theta}_i^* = -\dot{m}\psi_i^*\,.$$

By taking into account that

$$\tilde{\psi}_i = \gamma^*\psi_i^* + (1-\gamma^*)\,\psi_i^0\,,$$

one then has that

$$\left.\begin{aligned}\overline{M}_i^* = \overline{\Theta}_i^* + \overline{\Omega}_i^* = \frac{1}{2}\,(\dot{m}+|\dot{m}|)\,\psi_i^0 + \frac{1}{2}\,(\dot{m}-|\dot{m}|)\,\psi_i^* - \frac{\gamma^*\overline{\rho}\left(\psi_i^*-\tilde{\psi}_i\right)}{\tau^*\,(1-\gamma^*)}\,;\\ \overline{M}_i^0 = -\overline{M}_i^*\,.\end{aligned}\right\} \quad (11)$$

The proposed LES-EPaSR model can, hence, be summarized as follows. The filtered continuity and momentum equations (1_1) and (1_3), respectively, are solved together with the N species equations ($1\le i\le N$) and the energy equation ($i=N+1$), compactly expressed in Eq. (6_1). As an immediate consequence of the application of the multiphase analogy, it follows that $\overline{\dot{w}_i}\approx\gamma^*\overline{\dot{w}}_i^*$ for all $i\le N$, in which γ^* is the fine structure volume fraction and $\overline{\dot{w}}_i^*=\overline{\dot{w}}_i(\boldsymbol{\psi}^*)$ are the source terms of the species and energy equations, respectively, evaluated at the fine structure conditions, ψ^*. The conditions of the fine structures, ψ_i^*, are in this model evaluated by solving the fine structure balance equations (6_2) using the modeled exchange terms (11_1). To close Eqs. (6_1), (6_2), and (11_1), it is, hence, necessary also to provide closure models for the fine-structure volume fraction, γ^*, and the fine-structure residence time, τ^*. The fine-structure volume fraction is here obtained by solving the balance equation (9) in which the equilibrium fine-structure volume fraction, $\gamma_{\rm eq}^*$, however, needs to be provided by some additional closure model. The required closure models for τ^* and $\gamma_{\rm eq}^*$ will be developed later in subsection 3.4 and will be based also on the cartoon of turbulent combustion discussed in subsection 3.2 and illustrated in Fig. 1. In order to simplify the computational model, without violating the basic physics, and to avoid calculating the fine-structure density and velocity fields, ρ^* and $\tilde{\mathbf{v}}^*$,

in Eqs. (6_2) and (9), it is hereafter assumed that $\rho^* \approx \overline{\rho}$ and $\tilde{\mathbf{v}}^* \approx \tilde{\mathbf{v}}^{\mathbf{0}} \approx \tilde{\mathbf{v}}$ so that in the LES-EPaSR model the governing equations are

$$\left.\begin{aligned}
\partial_t\left(\overline{\rho}\tilde{\psi}_i\right) + \nabla\cdot\left(\overline{\rho}\tilde{\mathbf{v}}\tilde{\psi}_i\right) &= \nabla\cdot\left(\overline{\mathbf{k}}_i - \mathbf{b}_i\right) + \overline{\dot{\omega}}_i\,;\\
\partial_t\left(\overline{\rho}\gamma^*\psi_i^*\right) + \nabla\cdot\left(\overline{\rho}\gamma^*\psi_i^*\tilde{\mathbf{v}}\right) &= \nabla\cdot\left(\gamma^*\left(\overline{\mathbf{k}}_i - \mathbf{b}_i\right)\right) + \gamma^*\overline{\dot{\omega}}_i^*\\
+\frac{1}{2}\left(\dot{m}+|\dot{m}|\right)\psi_i^0 + \frac{1}{2}\left(\dot{m}-|\dot{m}|\right)\psi_i^* &- \frac{\gamma^*\overline{\rho}\left(\psi_i^* - \tilde{\psi}_i\right)}{\tau^*\left(1-\gamma^*\right)}\,;\\
\partial_t\left(\overline{\rho}\gamma^*\right) + \nabla\cdot\left(\overline{\rho}\gamma^*\tilde{\mathbf{v}}\right) &= -\frac{\overline{\rho}\left(\gamma^* - \gamma_{\mathrm{eq}}^*\right)}{\tau^*}\,;\\
\overline{\dot{\omega}}_i = \gamma^*\overline{\dot{w}}_i^*\,,\quad 1\le i\le N\,;&\\
\overline{\dot{w}}_{N+1} = \overline{\mathbf{S}}\cdot\nabla\tilde{\mathbf{v}} + \partial_t(\overline{p}) + \nabla\overline{p}\cdot\tilde{\mathbf{v}} &- \gamma^*\sum_{i=1}^{N}\left(\overline{\dot{w}}_i h_{f,i}^{\theta}\right)
\end{aligned}\right\} \qquad (12)$$

in which $\dot{m}$ is assumed to be provided by the linear model (8).

The LES-EPaSR model (12) can be simplified significantly by assuming that the convective and diffusive terms in (12_2) can be neglected which, in turn, implies that $\gamma^*\overline{\dot{\omega}}_i^* + \overline{\dot{M}}_i^* = 0$. Summing in this relation over $i \in [1,\ldots,N]$, taking into account that $\sum_i\left(\overline{\dot{\omega}}_i^*\right) = 0$, as follows from the law of mass action, it follows that $\sum_i\left(\overline{\dot{M}}_i^*\right) = 0$, which, by the definition of $\dot{m}$ as $\dot{m} = \sum_i\left(\overline{\dot{M}}_i^*\right)$, results in $\dot{m} = 0$. Using the linear model (8) results in $\gamma^* = \gamma_{\mathrm{eq}}^*$. The fact that $\dot{m} = 0$ when convection and diffusion can be neglected at the subgrid level in (12_2) further implies that $\overline{\Theta}_i^* = 0$, which implies that

$$\overline{\dot{M}}_i^* = \overline{\Omega}_i^* = -\frac{\gamma^*\overline{\rho}\left(\psi_i^* - \psi_i^0\right)}{\tau^*}\,.$$

Combining this relation with $\gamma^*\overline{\dot{\omega}}_i^* + \overline{\dot{M}}_i^* = 0$, making use of $\tilde{\psi}_i = \gamma^*\psi_i^* + \left(1-\gamma^*\right)\psi_i^0$, results in that

$$\frac{\overline{\rho}\left(\psi_i^* - \tilde{\psi}_i\right)}{\tau^*\left(1-\gamma^*\right)} = \overline{\dot{\omega}}_i^*\,,\quad 1\le i\le N\,,$$

so that Eqs. (12) become

$$\left.\begin{aligned}
\partial_t\left(\overline{\rho}\tilde{\psi}_i\right) + \nabla\cdot\left(\overline{\rho}\tilde{\mathbf{v}}\tilde{\psi}_i\right) &= \nabla\cdot\left(\overline{\mathbf{k}}_i - \mathbf{b}_i\right) + \dot{\overline{\omega}}_i\,; \\
\frac{\overline{\rho}\left(\psi_i^* - \tilde{\psi}_i\right)}{\tau^*\left(1-\gamma_{\mathrm{eq}}^*\right)} &= \dot{\overline{\omega}}_i^*\,; \\
\dot{\overline{\omega}}_i = \gamma_{\mathrm{eq}}^*\overline{w}_i^*\,, \quad 1 \le i \le N\,; & \\
\dot{\overline{\omega}}_{N+1} = \overline{\mathbf{S}}\cdot\nabla\tilde{\mathbf{v}} + \partial_t(\overline{p}) + \nabla\overline{p}\cdot\tilde{\mathbf{v}} - \gamma_{\mathrm{eq}}^*\sum_{i=1}^{N}\left(\overline{w}_i h_{f,i}^{\theta}\right)\,. &
\end{aligned}\right\} \tag{13}$$

The model (13) is easily recognized as the LES-PaSR model [12, 39] which then follows from simplifying the LES-EPaSR model (12). To close the LES-EPaSR and PaSR models (12) and (13), the models for γ_{eq}^* and τ^* are therefore required as will be discussed next.

3.4 Modeling the Subgrid Time and the Equilibrium Reacting Volume Fraction

To close the EPaSR and PaSR models, the subgrid time, τ^*, and reacting volume fraction, γ^*, need to be provided. In this subsection, the submodels for both these quantities are proposed based on the physical description of turbulent combustion at high Re and moderate Da numbers, provided in section 2 and Fig. 1.

To estimate the subgrid time, τ^*, let first observe that the fine scale structures in a volume, ΔV^*, are generally anisotropic (sheets, ribbons, and tubes) and influenced by the subgrid velocity stretch, v'/Δ, the characteristic time of which is Δ/v'. The smallest quasi-equilibrium scale of the fine structures, ℓ_D, is controlled by molecular viscosity and the characteristic time of the stretch Δ/v', such that $\ell_D = (\nu\Delta/v')^{1/2}$. Its similarity with the Taylor length scale, $\ell_T = (\nu\ell_I/v')^{1/2}$, defined from the molecular viscosity and the integral time scale ℓ_I/v', suggests that ℓ_D is the dissipative length scale of the smallest resolved scales. Let further assume that area-volume ratio, $\Delta S^*/\Delta V^*$, is solely determined by ℓ_D so that $\Delta S^*/\Delta V^* \approx 1/\ell_D$. For small deviations from the equilibrium state, a simple relaxation equation can be formulated for the variation of ΔV^* so that

$$\frac{d\left(\Delta V^*\right)}{dt} = -v_{\mathrm{K}}\left(\frac{\Delta S^*}{\Delta V^*}\right)_{\mathrm{eq}}\left(\Delta V^* - \Delta V_{\mathrm{eq}}^*\right) \tag{14}$$

in which we take into account that the change of the volume ΔV^* is due to the propagation of the surface ΔS^* with relative velocity on the order of the

Kolmogorov velocity, v_{K} [28]. From Eq. (14), it also becomes evident that the subgrid time scale may be expressed as

$$\tau^* = \left(v_{\mathrm{K}} \left(\frac{\Delta S^*}{\Delta V^*} \right)_{\mathrm{eq}} \right)^{-1} = \frac{\ell_D}{v_{\mathrm{K}}} \,. \tag{15}$$

Note also that Eqs. (14) and (15) degenerate into (9) when divided by ΔV. It should, however, be also noted that if it is assumed that area-volume density, $\Delta S^*/\Delta V^*$, is instead determined by the Kolmogorov scale, ℓ_{K}, one obtains $\tau^* = \tau_{\mathrm{K}}$, which contradicts the physical description of the fine structures discussed above. Using the definition of the Kolmogorov length and time scales, $\ell_{\mathrm{K}} = \left(\nu^3/\varepsilon\right)^{1/4}$ and $\tau_{\mathrm{K}} = \ell_{\mathrm{K}}/v_{\mathrm{K}}$, respectively, with $\varepsilon = \left(v'\right)^3/\Delta$ being the dissipation, this results in

$$\tau^* = \sqrt{\tau_{\mathrm{K}} \tau_\Delta}$$

where $\tau_\Delta = \Delta/v'$ is the subgrid velocity stretch time. This represents the geometrical mean of the Kolmogorov time and the time scale associated with the subgrid velocity stretch.

According to (4), the equilibrium reacting fine-structure fraction is defined as $\gamma^*_{\mathrm{eq}} = \Delta V^*/\Delta V$, which for LES actually translates into $\gamma^*_{\mathrm{eq}} = \Delta V^*/\Delta^3$ where Δ^3 denotes the local cell volume, in which all (resolved) LES variables ($\overline{\rho}$, $\tilde{\mathbf{v}}$, $\overline{p}$, $\tilde{T}$, $\tilde{Y}_i$, ...) can be assumed constant during each time step. This implies that one can lump the fine structure and surrounding fluid components together in different parts of the LES cell. The lumped fine structures are collectively described by the chemical time scale, τ_c, as the reactions are assumed to take place within these structures. Since the dependent variables can be assumed constant in each LES cell, the fine-structure volume can be estimated as $\Delta V^* = \Delta^2 \left|\tilde{\mathbf{v}}\right| \tau_c$. Similarly, the local cell volume can be estimated as $\Delta^3 = \Delta^2 \left|\tilde{\mathbf{v}}\right| \left(\tau_c + \tau^*\right)$ where $\tau_c + \tau^*$ is the flow-through time for each LES cell. This then finally results in that

$$\gamma^*_{\mathrm{eq}} = \frac{\tau_c}{\tau_c + \tau^*} \,. \tag{16}$$

The chemical time scale should be representative of the overall chemical reaction and although many options are available, here it is assumed that

$$\tau_c \approx \frac{\delta_u}{s_u} \approx \frac{\nu}{s_u^2}$$

where δ_u and s_u are the laminar flame thickness and flame speeds, respectively. By using the models $\tau^* = \sqrt{\tau_{\mathrm{K}} \tau_\Delta}$ (with $\tau_{\mathrm{K}} = \left(\nu/\varepsilon\right)^{1/2}$, $\varepsilon = \left(v'\right)^3/\Delta$, and $\tau_\Delta = \Delta/v'$) and $\tau_c \approx \nu/s_u^2$, Eq. (16) then becomes

$$\gamma^*_{\mathrm{eq}} = \frac{\nu^{3/4} v'^{5/4}}{s_u^2 \Delta^{3/4} + \nu^{3/4} v'^{5/4}} \,.$$

4 RELATIONS WITH OTHER LARGE EDDY SIMULATION TURBULENCE CHEMISTRY INTERACTION MODELS

The proposed LES-EPaSR model is next placed in perspective by comparison with contemporary LES combustion models such as, e. g., the LES-TFM, EDC, PaSR, and FPV models. The comparison is performed by, first, assessing the theoretical formulations of these models and, second, by comparing predictions of these models with experimental data, as will be presented in section 7. In addition to the continuity, momentum, and energy equations, the LES-TFM, EDC, PaSR, and EPaSR models depend on species equations of the form

$$\partial_t \left(\overline{\rho}\tilde{Y}_i\right) + \nabla \cdot \left(\overline{\rho}\tilde{Y}_i\tilde{\mathbf{v}}\right) = \nabla \cdot \left(\left(D_i + D_k\right)\nabla\tilde{Y}_i\right) + \overline{\dot{w}}_i$$

whereas the LES-FPV family of models makes use of an equation for a progress variable c (and a mixture fraction equation if appropriate) such that

$$\partial_t \left(\overline{\rho}\tilde{c}\right) + \nabla \cdot \left(\overline{\rho}\tilde{\mathbf{v}}\tilde{c}\right) = \nabla \cdot \left(D_k\nabla\tilde{c}\right) + \overline{\dot{w}}_c$$

where D_k is the subgrid diffusivity, and $\overline{\dot{w}_i}$ and $\overline{\dot{w}_c}$ are the reaction rate terms. Table 1 details D_k and $\overline{\dot{w}}$ terms for the models tested here. In these models, Ξ, F, and E are the flame wrinkling, flame thickening, and efficiency factors, respectively, γ^*_{PaSR}, $\gamma^*_{\mathrm{EPaSR}}$, and γ^*_{EDC} are the reacting volume fractions for the PaSR, EPaSR, and EDC models, respectively, whereas Y^*_k and T^* are the fine-structure species mass fractions and temperatures. For additional details, refer to the references and additional references therein. Regarding the LES-FPV models, a range of submodels for D_k and $\overline{\dot{w}_c}$ are available as reviewed by Ma *et al.* [41]. The individual variations in predictive capabilities between the eleven models

Table 1 The LES combustion model comparison

Model	Diffusivity	Reaction rate models	Flame wrinkling
FPV [40]	μ/Sc_T	$\rho_u s_u \Sigma = \rho_u S_u \Xi \left\|\nabla\overline{c}\right\|^*$	$\sigma/\left\|\nabla\overline{c}\right\| = \Xi^*$
TFM [11]	$(FE-1)D_i$	$(E/F)\dot{w}_i\left(\overline{\rho}, \tilde{Y}_k, \tilde{T}\right)$	$\sqrt{1+\min(\Delta/\delta_u, \Gamma v'/s_u)}$
PaSR [12]	μ/Sc_T	$\gamma^*_{\mathrm{PaSR}}\dot{w}^*_i\left(\overline{\rho}, \tilde{Y}_k, \tilde{T}, Y^*_k, T^*\right)$	$\sqrt{\gamma^*_{\mathrm{PaSR}}(1+D_k/D)}$
EPaSR	μ/Sc_T	$\gamma^*_{\mathrm{eq}}\dot{w}^*_i\left(\overline{\rho}, \tilde{Y}_k, \tilde{T}, Y^*_k, T^*\right)$	$\sqrt{\gamma^*_{\mathrm{eq}}(1+D_k/D)}$
EDC [6, 13]	μ/Sc_T	$\gamma^*_{\mathrm{EDC}}\dot{w}^*_i\left(\overline{\rho}, \tilde{Y}_k, \tilde{T}, Y^*_k, T^*\right)$	$\sqrt{\gamma^*_{\mathrm{EDC}}(1+D_k/D)}$

*Ξ is provided by a separate balance equation [40], with an equilibrium value of $\Xi = 1 + 2\tilde{c}(\theta - 1)$, with $\theta = 1 + 0.62\mathrm{Re}_{\mathrm{K}}\left(v'/s_u\right)^{1/2}$ where $\mathrm{Re}_{\mathrm{K}} = v' l_{\mathrm{K}}/\nu$ is the Kolmogorov-based Reynolds number.

compared in [41] are small, with a few exceptions, and based on the recommendations in [41], here, the model of Weller *et al.* [40] is used as a representative. In the LES-TFM model, a term similar to the reacting volume fraction, E/F, appears, although having a somewhat different interpretation that may, according to [11], be reformulated as $E/F = \Xi_\Delta/F$, in which now

$$\Xi_\Delta = \sqrt{1 + \min\left(\frac{\Delta}{\delta_u}, \frac{\Gamma v'}{s_u}\right)}$$

is the resolved flame wrinkling and Γ is the efficiency function of Charlette *et al.* [11], to account for the net straining at subgrid scales. Regarding the expressions for the reacting volume fractions, both PaSR and EPaSR use the same baseline (i. e., equilibrium) model, $\gamma^*_{\mathrm{PaSR}} = \gamma^*_{\mathrm{eq}} = \tau_c/(\tau_c + \tau^*)$, which may be reformulated as

$$\gamma^*_{\mathrm{PaSR}} = \gamma^*_{\mathrm{eq}} = \frac{\nu^{3/4} v'^{5/4}}{s_u^2 \Delta^{3/4} + \nu^{3/4} v'^{5/4}}.$$

For the EDC model [6, 13], $\gamma^*_{\mathrm{EDC}} = (v^*/v')^3$, which may, according to [6], be conveniently reformulated as $\gamma^*_{\mathrm{EDC}} = 1.02\,(\nu/\Delta v')^{3/4}$. To compare the models in Table 1, a laminar flame speed analogy in which $s_L \approx \sqrt{D\dot{w}/\rho^2}$ is employed so that

$$s_T \approx \sqrt{\frac{(D + D_k)\,\overline{\dot{w}}}{\rho^2}}$$

which typically results in $s_T = \Xi s_u$ where Ξ is the flame wrinkling factor as included in Table 1 for the different models. This comparison can only be approximate due to the necessary assumptions, and a more comprehensive comparison is provided in section 7 where the predictions using the models listed in Table 1 are compared for a lean-premixed bluff-body stabilized flame for which high-quality experimental data of velocity, temperature, and some species are available for comparison.

5 GLOBAL HYDROCARBON COMBUSTION CHEMISTRY

Accurate predictions of temperature and species concentrations require the use of carefully selected reduced reaction mechanisms, and in this study, a reduced three-step mechanism for C_3H_8–air combustion is used. The mechanism is detailed in Table 2, for which the Arrhenius coefficients have been optimized to match the laminar flame speeds and temperatures of the San Diego mechanism for lean-premixed flames [42]. The third reaction step, modeling NO formation, is the sum of two rates, one for thermal NO (only dependent on temperature) and

Table 2 Rate parameters for the reduced three-step C_3H_8–air mechanisms

Reaction	A, m, kg, mol, s	n	$b_{C_3H_8}$	b_{O_2}	n_{CO}	T_a, K
$C_3H_8 + 3.5O_2 \rightarrow 3CO + 4H_2O$	$3.62 \cdot 10^9$	0.93	0.36	1.75		18,590
$CO + 0.5O_2 \leftrightarrow CO_2$	$2.14 \cdot 10^6$	0.87		0.83	0.55	12,710
$O_2 + N_2 \rightarrow 2NO$	$1.50 \cdot 10^{16}$	−0.30				38,440

one for prompt NO (depending on the hydrocarbon fuel and H_2O). Most of NOx reacts to NO_2 after combustion; however, close to the flame, NO is dominant, and hence, it is sufficient to limit the mechanism to NO. Associated with the reaction mechanism is the treatment of molecular diffusion, which is simplified and based on species Schmidt numbers so that $\overline{\mathbf{j}}_i \approx (\mu/\mathrm{Sc}_i)\nabla\tilde{Y}_i$ where the values of the individual species Schmidt numbers are listed in Table 3. For a critical evaluation and discussion of this approach to model the molecular diffusion refer to Giacomazzi *et al.* [43].

Table 3 Schmidt numbers

Specie	Sc_i
CH_4	0.68
C_3H_8	0.72
O_2	0.76
CO	0.76
CO_2	0.98
H_2O	0.60
N_2	0.75

Figures 2*a* and 2*b* present the variation of the adiabatic flame temperature (T_{ad}) and laminar flame speed (s_u) for the C_3H_8–air mechanism in Table 2. As reference for the reduced C_3H_8–air mechanism, the San Diego mechanism [42] was used. In addition, several experimental data sets [44–46] have been incorporated. Good agreement between the reduced and detailed mechanisms as well as with the experimental data is found for equivalence ratios (ϕ) less than 1.2, whereas for higher equivalence ratios, better mechanisms are needed. The flames

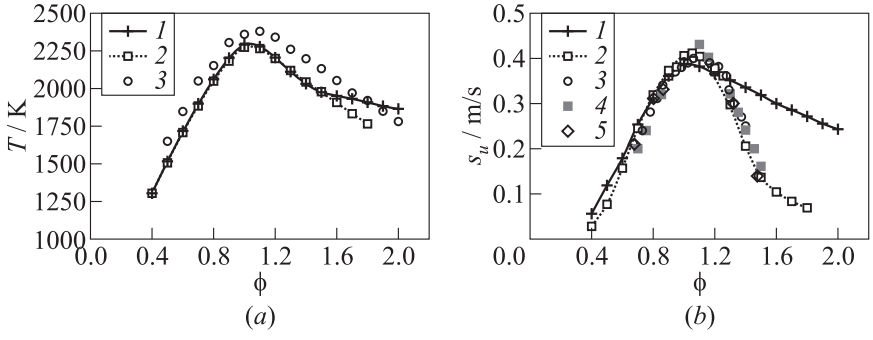

Figure 2 Comparison of adiabatic flame temperatures (*a*) and flame velocities (*b*) for the C_3H_8–air mechanism (see Table 2): *1* — two-step reduced C_3H_8–air mechanism; *2* — C_3H_8 [42], detailed reaction mechanism; *3* — C_3H_8–air, experiments [44]; *4* — C_3H_8–air, experiments [45]; and *5* — C_3H_8–air, experiments [46]

considered here are all lean flames, justifying using the reduced mechanism of Table 2.

6 NUMERICAL METHOD

For this investigation, the authors use the C++ library OpenFoam [47] as the computational platform, which has previously been used for applications of varying complexity. The code employs an unstructured collocated Finite Volume (FV) method [47] in which the discretization is based on Gauss theorem together with a semi-implicit time-integration scheme. Given the vector of unknowns, $\overline{\mathbf{u}} = \left[\overline{\rho}, \overline{\rho}\tilde{Y}_i, \overline{\rho}\tilde{\mathbf{v}}, \overline{\rho}\tilde{E}\right]^{\mathrm{T}}$, the semidiscretized equations are

$$\partial_t \left(\overline{\mathbf{u}}_P\right) + \frac{1}{\delta V_P} \sum_f \left[\mathbf{F}_f^C \left(\overline{\mathbf{u}}\right) - \mathbf{F}_f^D \left(\overline{\mathbf{u}}\right) + \mathbf{F}_f^B \left(\mathbf{u}, \overline{\mathbf{u}}\right)\right] = s_P \left(\mathbf{u}, \overline{\mathbf{u}}\right)$$

in which

$$\begin{aligned}
\mathbf{F}_f^C \left(\overline{\mathbf{u}}\right) &= \left[\overline{\rho}\tilde{\mathbf{v}}, \overline{\rho}\tilde{\mathbf{v}} \otimes \mathbf{v}, \overline{\rho}\tilde{\mathbf{v}}E, \overline{\rho}\tilde{\mathbf{v}}Y_i\right]^{\mathrm{T}} \, d\mathbf{A}_f \,; \\
\mathbf{F}_f^D \left(\overline{\mathbf{u}}\right) &= \left[0, \overline{p}\mathbf{I} - \overline{\mathbf{S}}, \overline{\rho}\tilde{\mathbf{v}}\tilde{E} + \overline{p}\tilde{\mathbf{v}} - \overline{\mathbf{S}}\tilde{\mathbf{v}} - \overline{\mathbf{h}}, -\overline{\mathbf{j}_i}\right]^{\mathrm{T}} \, d\mathbf{A}_f \,; \\
\mathbf{F}_f^B \left(\overline{\mathbf{u}}\right) &= \left[0, \mathbf{B}, \mathbf{b}, \mathbf{b}_i\right]^{\mathrm{T}} \, d\mathbf{A}_f \,; \\
s_p \left(\mathbf{u}, \overline{\mathbf{u}}\right) &= \left[0, \mathbf{0}, \overline{\rho}\tilde{\sigma}, \overline{\dot{w}_i}\right]^{\mathrm{T}}
\end{aligned}$$

are the convective, diffusive, subgrid fluxes and source terms, respectively. For the convective fluxes, $\mathbf{F}_f^C \left(\overline{\mathbf{u}}\right)$, a monotonicity preserving reconstruction

$$\mathbf{F}_f^C \left(\overline{\mathbf{u}}\right) = \mathbf{F}_f^{C,H} \left(\overline{\mathbf{u}}\right) - \left(1 - \Psi \left(\overline{\mathbf{u}}\right)\right) \left[\mathbf{F}_f^{C,H} \left(\overline{\mathbf{u}}\right) - \mathbf{F}_f^{C,L} \left(\overline{\mathbf{u}}\right)\right]$$

is employed [48] in which $\mathbf{F}_f^{C,H} \left(\overline{\mathbf{u}}\right)$ denotes the second-order linear reconstruction, $\mathbf{F}_f^{C,L} \left(\overline{\mathbf{u}}\right)$ the first-order upwind biased reconstruction, and $\Psi = \Psi(\overline{\mathbf{u}})$ a nonlinear flux limiter. The nonlinear flux limiter is used to switch between the two underlying reconstruction algorithms, and here, the Monotonized Central (MC) limiter [49] is used for the momentum, energy, and species transport equations whereas only the higher order scheme is used for the continuity equation. To minimize the nonorthogonality errors in the viscous and subgrid fluxes, $\mathbf{F}_f^D \left(\overline{\mathbf{u}}\right)$ and $\mathbf{F}_f^B \left(\overline{\mathbf{u}}\right)$, respectively, these are divided into orthogonal and nonorthogonal parts [48]. Central difference approximation and gradient face interpolation are used for the orthogonal and nonorthogonal parts, respectively. A second-order accurate semiimplicit Crank–Nicholson time-integration scheme is used together

with a PISO-like (Pressure Implicit with Splitting of Operators) algorithm, in the spirit of Rhie and Chow, for the cell-centered data storage structure [50]. Stability is imposed using compact stencils and by enforcing conservation of mass and kinetic energy. The equations are solved sequentially, with iteration over the nonlinear source terms to obtain rapid convergence, with a fixed CFL (Courant–Friedrichs–Lewy) number of about 0.4.

7 LARGE EDDY SIMULATION OF A BLUFF-BODY STABILIZED FLAME

The Volvo Validation Rig [51–53] is used as a target combustor due to the wealth of available experimental data, including high-speed imaging, gas analysis, LDV and CARS measurements, and the frequent use of this configuration in computational studies (see, e. g., [54, 55]). The rig consists of a rectilinear channel with a rectangular cross section, divided into an inlet section and a combustor section (Fig. 3). Gaseous propane (C_3H_8) is injected and premixed with the air upstream of the combustor section, resulting in a lean ($\phi = 0.62$) premixed flame stabilized behind a wedge-shaped flameholder of height $h = 0.04$ m. The combustion section discharges into a large diameter circular duct.

The case considered here is characterized by an inflow pressure of 101 kPa, an inflow velocity of 17 m/s, and an inflow temperature of 288 K, resulting in a Reynolds number of 46,000, a Karlowitz number of 1.1, and a Damköhler number of 9.5. Three computational grids have been generated with 2.00, 6.75, and 16.0 million cells, respectively. These three grids have the same topology, being refined towards the upper and lower walls, and around the wedge-shaped flameholder and the downstream following shear layers. In this study, only the

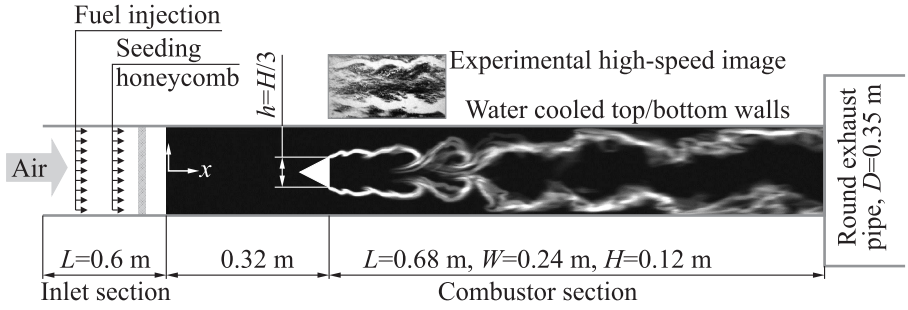

Figure 3 A schematic illustration of the Volvo Validation Rig used in the present study. Included is a frame from a high-speed video showing the symmetric and regular rollup of the shear layers together with a numerical schlieren image

results from the intermediate grid are presented as this grid has been found to result in predictions virtually identical to that of the fine grid, whereas the coarse grid shows the results that deviate slightly from the results obtained on the finer grids. At the inlet of the computational domain, the Dirichlet conditions are used whereas at the outlet, the wave-transmissive conditions [56] are used to emulate the dump tank in the experiments. Isothermal no-slip wall boundary conditions are used on the upper and lower walls of the combustor and on the flameholder. In the spanwise direction, the periodic boundary conditions are employed on the lateral sides of the computational domain being 0.12 m wide.

Figure 4 presents perspective views of the flame, in terms of an isosurface of the temperature, $\tilde{T}$, and contours of the CO mass fraction field, $\tilde{Y}_{\mathrm{CO}}$, and the flow, in terms of contours of the axial velocity, $\tilde{v}_x$, and an isosurface of the second invariant of the intermediate eigenvalue, λ_2, of the tensor $\tilde{\mathbf{D}}^2 + \tilde{\mathbf{W}}^2$. Here, $\tilde{\mathbf{D}}$ and $\tilde{\mathbf{W}}$ are the symmetric and skew-symmetric components of $\nabla\tilde{\mathbf{v}}$, respectively [57]. Both results from the conventional LES-TFM model (with $F = 3$) and the proposed LES-EPaSR models are included to exemplify both similarities and differences between these models. All models predict that the flame anchors behind the flameholder due primarily to recirculation of hot combustion products in the wake of the flameholder. All LES models compared predict symmetric shedding of spanwise $\tilde{\omega}_3$-vortices of the upper and lower corners of the flameholder, resulting in two, initially symmetric, flame brushes that separate cold reactants from hot combustion products. See, also, the high-speed video image and the numerical schlieren images in Fig. 3. Within each of these flame brushes, the separating vorticity comes off the flameholder rollup, generating a flow that locally wraps the flame around these regions of intense spanwise $\tilde{\omega}_3$-vorticity, resulting in an originally undulous flame. Longitudinal $\tilde{\omega}_{12}$-vortices develop simultaneously with perturbations of recently shed $\tilde{\omega}_3$-vortices in regions of intense strain, and further downstream, both these vortex structures are modified by vortex stretching, volumetric expansion, baroclinic torque, temperature-dependent molecular diffusion and subgrid diffusion. Due to these modifications of the vorticity, the flame brushes, and their internal structure, also loose their initial symmetry and undulous shape and become increasingly distorted, with the far downstream flame brushes being gradually more and more distorted, furrowed and wrinkled. The majority of the chemical reactions occurs on the (outer) fuel-rich side of the undulous and wrinkled shear layers, where most of the mixing between cold reactants and hot combustion products also take place. Isosurfaces of the heat-release

$$\dot{Q} = -\sum_{i=1}^{N} \left(\overline{\dot{w}_i} h_{f,i}^{\theta}\right)$$

(not shown) reveal a topologically complex structure embedded in the flame brush, consisting of contorted sheets and blobs or filaments of akin to those

shown in Fig. 1. Compared to non-reacting LES (not shown) and the laboratory measurement data [51–53], the volumetric expansion due to the heat release results in a longer and slightly wider region of reversed flow, followed by an acceleration of the flow towards the outlet.

As evident from Fig. 4, the LES-TFM and LES-EPaSR models predict both the flow and flame differently. These two results are representative of the two classes of predictions observed: the LES-TFM and LES-FPV result in an initially weakly undulous flame whereas the LES-EDC, LES-PaSR, and LES-EPaSR re-

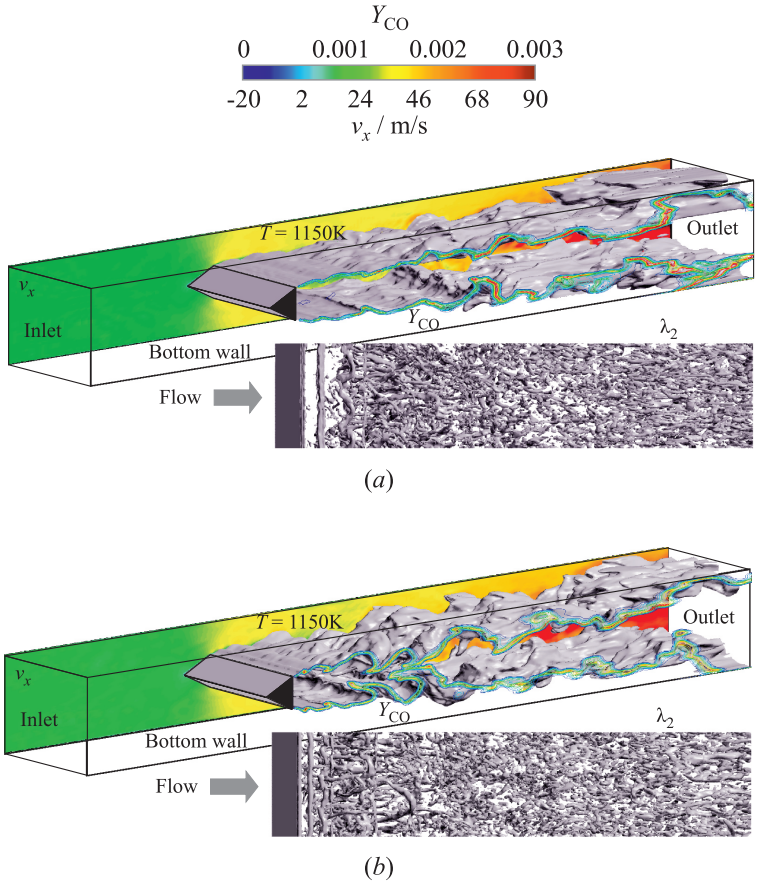

Figure 4 Perspective views of the flame, in terms an isosurface of the temperature at $\tilde{T} = 1150$ K and contours of the CO mass fraction field $\tilde{Y}_{CO}$, and the flow, in terms of contours of the axial velocity, $\tilde{v}_x$, and an isosurface of the second invariant of the second invariant of the second-largest eigenvalue, λ_2, of the tensor $\tilde{D}^2 + \tilde{W}^2$ for LES-TFM (a) and LES-EPaSR (b).

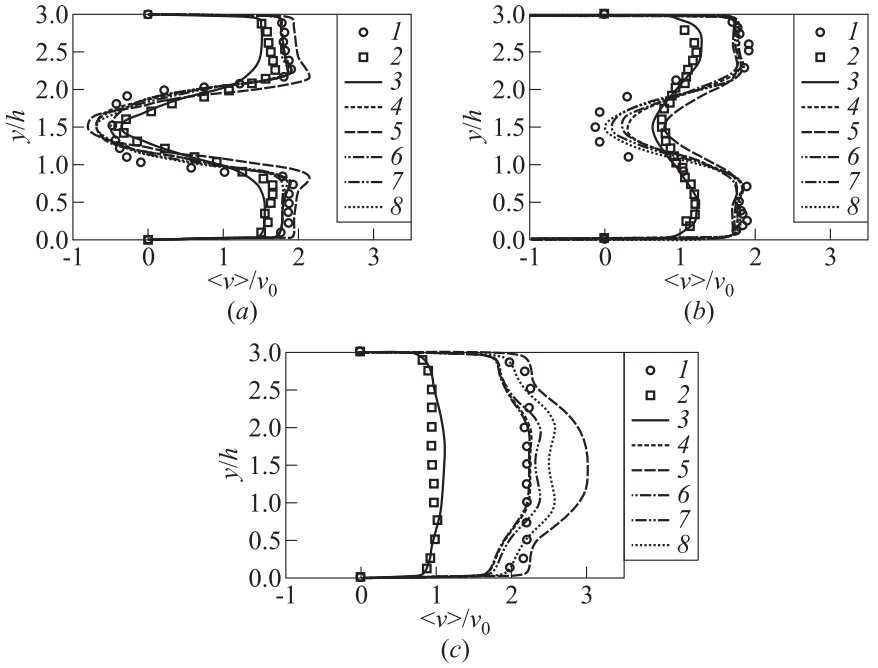

Figure 5 Time averaged axial velocity profiles at $x/h = 0.95$ (a), 3.75 (b), and 9.40 (c): *1* — LDV experimental data for the reacting case [53]; *2* — experimental data for the nonreacting case [51]; *3* — LES of the nonreacting case; *4* — LES-TFM; *5* — LES-FPV; *6* — LES-EDC; *7* — LES-PaSR; and *8* — LES-EPaSR of the reacting case

sult in an initially strongly undulous flame. Due to the interactions with the $\tilde{\omega}_3$ and $\tilde{\omega}_{12}$ vortices, the flame looses its original symmetry and becomes increasingly distorted, furrowed, and wrinkled as the distance from the flameholder increases. One explanation for the difference in behavior observed in Fig. 4 is offered by examining the turbulent flame speed, s_T. For high and low values of s_T the flame will be located outside of or inside the initial shear layers (composed of the $\tilde{\omega}_3$- and $\tilde{\omega}_{12}$-vortex structures) resulting in an initially weakly undulus flame. If instead s_T takes intermediate values, the flame will primarily coincide with the shear layers, resulting in an initially strongly undulus flame. High-speed video recordings of the experiments [53] included in Fig. 3, reveal initial strong undulations of the flame, supporting the results of the LES-EDC, LES-PaSR, and LES-EPaSR models.

Figure 5 presents the comparisons of the time-averaged axial velocity, $\langle \tilde{v}_x \rangle$, at $x/h = 0.95$, 3.75, and 9.40 downstream of the flameholder from the LES-TFM, LES-FPV, LES-EDC, LES-PaSR, and LES-EPaSR models with exper-

imental data [51–53]. The present authors were the first to observe that all five LES predictions resulted in a longer and wider recirculation region, and thus, a more gradual dissipation of momentum in the wake than the nonreacting cases. Close to the flameholder (at $x/h = 0.95$), the nonreacting experimental data and the nonreacting LES both result in a V-shaped $\langle \tilde{v}_x \rangle$ profile, whereas the reacting experimental data results in a U-shaped $\langle \tilde{v}_x \rangle$ profile. The reacting LES are observed to capture the U-shaped $\langle \tilde{v}_x \rangle$ profile with different degree of precision: the LES-FPV model results in a V-shaped $\langle \tilde{v}_x \rangle$ profile whereas the LES-PaSR model shows the most accurate agreement with the experimental results. Further downstream, in the velocity recovery region, at $x/h = 3.75$, the most perceptible differences between the experimental data and the computational results occur. In this region, the flow shows strong evidence of streamline contraction [58] and the flame then typically responds to this effect by widening slower. At this cross section, the LES-FPV model predicts a too shallow velocity defect, resulting from a too short recirculation region and a too rapid velocity increase. Between the remaining models, the LES-PaSR and LES-EPaSR models show the best agreement with the experimental data. At the most downstream location, in the fully developed turbulent flame section, the LES-FPV model overpredicts $\langle \tilde{v}_x \rangle$ in the core region, whereas close to the walls, this model results in reasonable predictions.

All other models demonstrate stronger cross-sectional variations than that is found in the experimental data. Best overall agreement is found for LES-EPaSR and LES-PaSR, whereas both LES-TFM and LES-EDC are observed to somewhat underpredict the time-averaged axial velocity.

Figure 6 presents the comparisons of the time-averaged temperature, $\langle \tilde{T} \rangle$, at $x/h = 0.95$, 3.75, and 9.40 downstream of the flameholder from LES-TFM, LES-FPV, LES-EDC, LES-PaSR, and LES-EPaSR models with experimental data [51–53]. Here, the experimental CARS data [53] at $x/h = 0.95$, 3.75, and 9.40 are compared with gas analysis data [51] at $x/h = 0.95$, 3.75, and 8.75. Note that the experimental data at the far downstream location from CARS and gas analysis are not collected at the same cross section, with the CARS data obtained at the same axial position as $\langle \tilde{v}_x \rangle$ of Fig. 5. At $x/h = 0.95$, satisfactory agreement is obtained between both experimental profiles and all five LES profiles, with the LES-FPV model profile being marginally sharper and predicting a slightly higher temperature. At $x/h = 3.75$, considerable differences are observed between the two experimental data sets, with the CARS profile being significantly narrower than the gas analysis profile. In [53], it is argued that the CARS data are more accurate than the gas analysis data since the samples employed in the gas analysis temperature measurements continue to react in the sampling tubes, thus overpredicting $\langle \tilde{T} \rangle$.

All LES predictions agree well with the CARS data, with the LES-EPaSR showing virtually perfect agreement whilst the other models, particularly, the

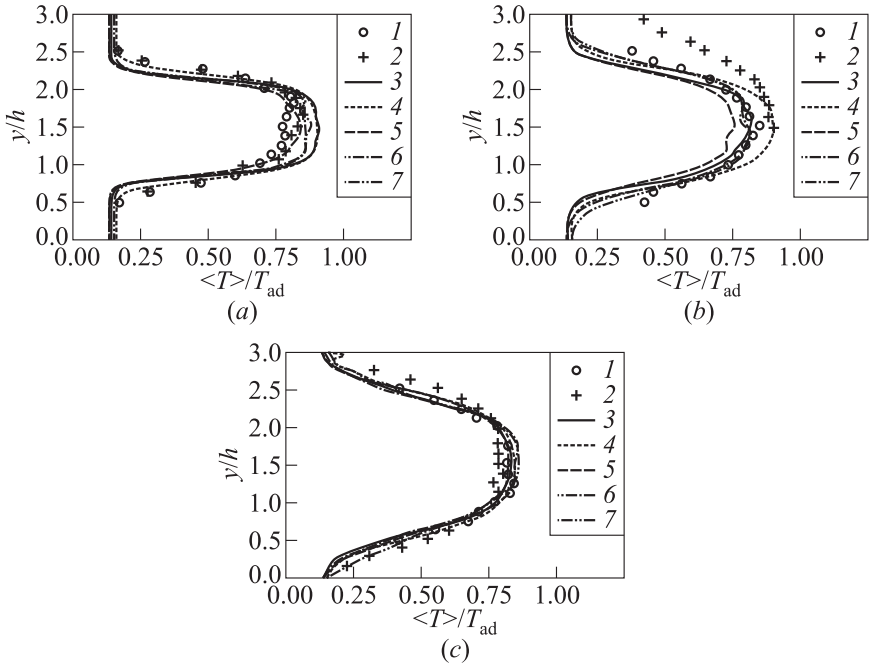

Figure 6 Time-averaged temperature profiles at $x/h = 0.95$ (a), 3.75 (b), and 9.40 (c): *1* — CARS experimental data [53]; *2* — gas analysis experimental data [51]; *3* — LES-TFM; *4* — LES-FPV; *5* — LES-EDC; *6* — LES-PaSR; and *7* — LES-EPaSR

LES-FPV and LES-TFM models, predict a too narrow and high $\langle \tilde{T} \rangle$ profile. Further downstream, at $x/h = 9.40$, the CARS and gas analysis based $\langle \tilde{T} \rangle$ profiles agree well with each other. At this cross section, all of the LES models investigated show good agreement with the experimental data but with the LES-EPaSR model showing somewhat better agreement with the experimental results towards the upper and lower walls.

Figure 7 presents the comparisons of the time-averaged CO mass fraction, $\langle \tilde{Y}_{\mathrm{CO}} \rangle$, at $x/h = 0.95$, 3.75, and 8.75 downstream of the flameholder from LES-TFM, LES-EDC, LES-PaSR, and LES-EPaSR models with experimental data [49–51]. At the first location, $x/h = 0.95$, good agreement between the experimentally measured and predicted $\langle \tilde{Y}_{\mathrm{CO}} \rangle$ profiles can generally be observed for all LES models. However, the peak $\langle \tilde{Y}_{\mathrm{CO}} \rangle$ values, occurring in the upper and lower shear layers, are predicted differently by the different models, and here, the LES-EDC model presents the best overall agreement.

More important is the prediction of $\langle \tilde{Y}_{\mathrm{CO}} \rangle$ in the hot combustion products just behind the flameholder which only the LES-PaSR and LES-EPaSR models

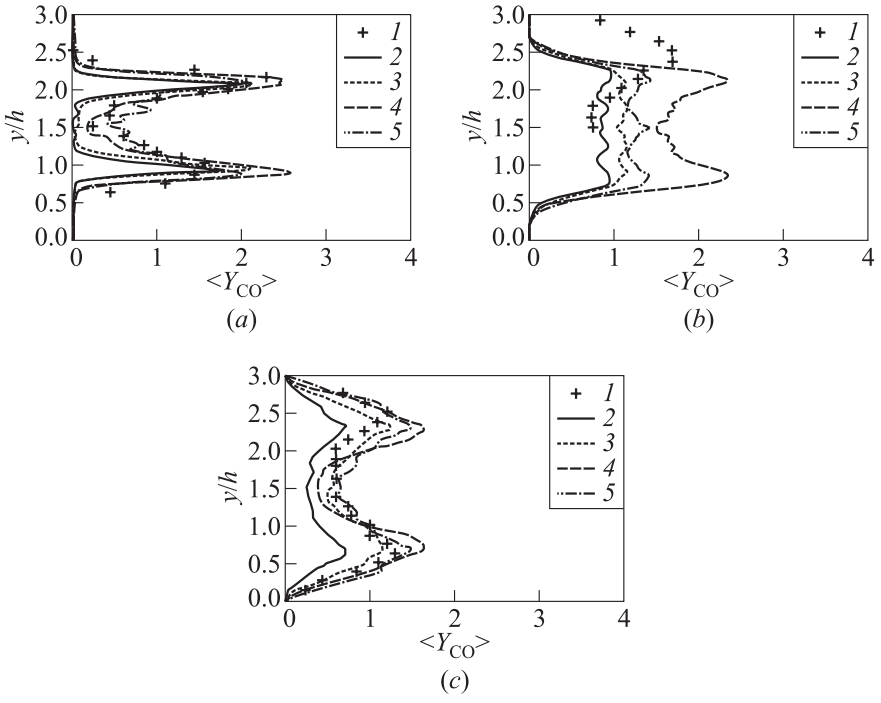

Figure 7 Time-averaged CO mass fraction profiles at $x/h = 0.95$ (a), 3.75 (b), and 9.40 (c): *1* — gas analysis experimental data [51]; *2* — LES-TFM; *3* — LES-EDC; *4* — LES-PaSR; and *5* — LES-EPaSR

can capture reasonably well. At $x/h = 3.75$, the discrepancies between the measurement data and the LES predictions are considerably larger, with also more divergent differences between the model predictions. The assumed reason for this difference is the same as previously discussed for $\langle\tilde{T}\rangle$, originating in potential problems with the gas analysis sampling, allowing chemical reaction to take place also outside of the combustor, in the probe itself. This would then partially invalidate the experimental results for $\langle\tilde{Y}_{\mathrm{CO}}\rangle$, and by comparing the evolution of the measured $\langle\tilde{Y}_{\mathrm{CO}}\rangle$ profiles along the combustor, it seems plausible that there may be a more severe problem with the experimental data at $x/h = 3.75$, which then should be treated with additional care. For this cross section, the LES-EDC and LES-EPaSR models compare well with each other, whereas the LES-TFM and LES-PaSR models show lower and higher values of $\langle\tilde{Y}_{\mathrm{CO}}\rangle$, respectively. At $x/h = 8.75$, the LES-EDC and LES-EPaSR models show overall best agreement with the experimental data closely followed by the LES-PaSR model, whereas the LES-TFM model underpredicts $\langle\tilde{Y}_{\mathrm{CO}}\rangle$.

8 SUMMARY AND CONCLUDING REMARKS

This paper proposes a novel LES finite rate chemistry combustion model for turbulent flows. The developing this model was started from a simple cartoon of turbulent flow (subsequently also involving combustion) that has evolved ever since Kolmogorov proposed his 1941 theory [23]. This cartoon is based on the evolving turbulence theory [23, 24], DNS data (see, e. g., [20]), its extension to turbulent combustion [13, 16, 17, 37], and combustion DNS data (see, e. g., [21, 22]), and may be summarized as follows. A turbulent reacting flow is characterized by nonuniform spatial distribution of velocity gradients, molecular mixing, and dissipation. Regions of high intensity often concentrate in elongated filaments embedded into sheets or arcs of lower intensity, whose complete volume is a fraction of the whole volume, increasing with increasing cell Reynolds number, Re_Δ. Recent DNS (see, e. g., [21, 22]) support this cartoon and suggest that the fine structures at the flame are mainly parallel to the flame whereas those behind the flame are typically perpendicular to the flame. The regions of heat release and volumetric expansion are found to be distributed among the fine-structure vortices in a background of low heat release and volumetric expansion.

The idea of the proposed model is to use the mathematical treatment of multiphase flows for the description of fine-scale structures dissolved in a background turbulence, characterized by lower intensity mixing. The approach results in a model closure of the filtered reaction rates, $\overline{\dot{w}_i(\rho, T, Y_k)}$, of the form $\overline{\dot{w}_i(\rho, T, Y_k)} = \gamma^* \dot{w}_i(\overline{\rho}, T^*, Y_k^*)$ in which $\{Y_i^*, T^*\}$ denotes the fine structure conditions and γ^* the fine structure volume fraction. In the LES-EPaSR model, $\{Y_i^*, T^*\}$ are obtained by solving a set of transport equations, being more general and versatile than the LES-PaSR model, in which $\{Y_i^*, T^*\}$ were obtained from local algebraic equations, obtained from the transport equations if subgrid convection is assumed negligible. Based on the multiphase analogy, a separate transport equation for γ^* results that is of the form $\partial_t (\overline{\rho}\gamma^*) + \nabla \cdot (\overline{\rho}\gamma^* \tilde{\mathbf{v}}) = -\overline{\rho} \left(\gamma^* - \gamma_{\mathrm{eq}}^*\right) / \tau^*$, in which γ_{eq}^* is the equilibrium fine-structure volume fraction and τ^* the subgrid time scale. The submodels proposed here for γ_{eq}^* and τ^* are based primarily on geometrical considerations, resulting in that $\tau^* = \sqrt{\tau_{\mathrm{K}} \tau_\Delta}$ and $\gamma_{\mathrm{eq}}^* = \tau_c / (\tau_c + \tau^*)$, in which τ_{K} is the Kolmogorov time scale, τ_Δ is the time scale of the resolved shear, and τ_c is the chemical time scale $\tau_c \approx \nu / s_u^2$. This particular time scale was recently found by Yeung *et al.* [59] to be the time scale that most accurately characterized the Lagrangian statistics of dissipation, and therefore, this time scale also appears as a reasonable choice for representing the subgrid processes of interest to mixing and combustion at high Reynolds numbers.

The proposed model, hereafter referred to as the LES-EPaSR model, was then successfully evaluated against other well-known LES combustion models such as the LES-PaSR, LES-EDC, LES-TFM, and LES-FPV models for a high Reynolds number turbulent lean-premixed bluff-body stabilized flame. Experimental data,

including high-speed imaging and time-averaged axial velocity, temperature, and CO mass fraction, were used to provide the reference against which the proposed LES model could be bechmarked together with the well-known LES models. Guided by the high-speed imaging, which reveals initial strong undulations of the flame, it was found that only the LES-EDC, LES-PaSR, and LES-EPaSR models have the capacity to capture this particular behavior whereas the LES-TFM and LES-FPV results in an initially weakly undulus flame. Further downstream, the undulus flame interacts with the coupled spanwise and longitudinal vorticity to gradually develop a distorted, furrowed, and wrinkled flame. Comparison of time-averaged axial velocity, temperature, and CO mass fractions from experiments and LES predictions shows that no single LES model is superior in all instances but by considering the whole dataset the overall best performing model may be identified. For this combustor, the overall best performing model is the LES-EPaSR model, closely followed by the LES-PaSR model. The LES-FPV model is the least accurate performing model, whereas the LES-TFM and LES-EDC models provide intermediate agreement with the experimental data.

ACKNOWLEDGMENTS

Financial support for this work was provided by the Office National d'Etudes et de Recherches Aerospatiales (VS) and by the Swedish Armed Forces (CF). Helpful discussion with A. Mura and his comments are gratefully acknowledged.

REFERENCES

1. Poinsot, T., and D. Veynante. 2001. *Theoretical and numerical combustion*. Ed. R. T. Edwards. Philadelphia.
2. Sagaut, P. 2001. *Large eddy simulation for incompressible flows*. Heidelberg: Springer Verlag.
3. Grinstein, F. F., L. Margolin, and B. Rider, eds. 2007. *In implicit large eddy simulation: Computing turbulent fluid dynamics*. Cambridge University Press.
4. Janicka, J., and A. Sadiki. 2005. Large eddy simulation of turbulent combustion systems. *Proc. Combust. Inst.* 30:537.
5. Pitsch, H. 2006. Large eddy simulation of turbulent combustion. *Annu. Rev Fluid Mech.* 38:453.
6. Fureby, C. 2008. LES modeling of combustion for propulsion applications. *Phil. Trans. R. Soc. A* 367:2957.
7. Wang, P., and X. S. Bai. 2005. Large eddy simulation of turbulent premixed flames using level-set G-equation. *Proc. Combust. Inst.* 30:583.

8. Hawkes, E. R., and R. S. Cant. 2000. A flame surface density approach to large eddy simulation of premixed turbulent combustion. *Proc. Combust. Inst.* 28:51.
9. Knikker, R., and D. Veynante. 2000. Experimental study of the filtered progress variable approach for LES of premixed combustion. In: *Advances in LES of complex flows*. Eds. R. Friedrich and W. Rodi. 353.
10. Givi, P. 2006. Filtered density function for subgrid scale modeling of turbulent combustion. *AIAA J.* 44:16.
11. Charlette, F., C. Meneveau, and D. Veynante. 2002. A power-law flame wrinkling model for LES of premixed turbulent combustion. Part I: Non-dynamic formulation and initial tests. *Combust. Flame* 131:159.
12. Berglund, M., E. Fedina, J. Tegnér, C. Fureby, and V. Sabelnikov. 2010. Finite rate chemistry LES of self-ignition in a supersonic combustion ramjet. *AIAA J.* 48:540.
13. Magnussen, B. F. 1981. On the structure of turbulence and a generalised eddy dissipation concept for chemical reactions in turbulent flow. *19th AIAA Sc. Meeting*. St. Louis, USA.
14. Bilger, R. W. 1993. Conditional moment closure for turbulent reacting flow. *Phys. Fluids A* 5:436.
15. Sankaran, V., and S. Menon. 2005. Subgrid combustion modeling of 3D premixed flames in the thin-reaction-zone regime. *Proc. Combust. Inst.* 38:575.
16. Chomiak, J. 1970. A possible propagation mechanism of turbulent flames at high Reynolds numbers. *Combust. Flame* 15:319.
17. Chomiak, J. 1979. Basic considerations in the turbulent flame propagation in premixed gases. *Prog. Energy Combust. Sci.* 5:207.
18. Ertesvåg, I. S., and B. F. Magnussen. 2000. The eddy dissipation turbulence energy cascade model. *Combust. Sci. Tech.* 159:213.
19. Batchelor, G. K., and A. A. Townsend. 1949. The nature of turbulent motion at large wave-numbers. *Proc. Roy. Soc. London A* 199:238.
20. Woodward, P. R., D. H. Porter, I. Sytine, S. E. Anderson, A. A. Mirin, B. C. Curtis, R. H. Cohen, W. P. Dannevik, A. M. Dimits, D. E. Eliason, K.-H. Winkler, and S. W. Hodson. 2001. Very high resolution simulations of compressible turbulent flows. *Computational fluid dynamics. 4th UNAM Supercomputing Conference Proceedings*. Eds. E. Ramos, Cisneros G., Fernandez-Flores A., and Santillan-Gonzalez A. World Scientific. 3.
21. Tanahashi, M., M. Fujimura, and T. Miyauchi. 2000. Coherent fine scale eddies in turbulent premixed flames. *Proc. Combust. Inst.* 28:5729.
22. Tanahashi, M., M. Sato, M. Shimura, and T. Miyauchi. 2008. DNS and combined laser diagnostics of turbulent combustion. *J. Thermal Sci. Tech.* 3:391.
23. Kuo, Y. S., and S. Corrsin. 1971. Experiments on internal intermittency and fine structures distribution functions in fully turbulent fluid. *J. Fluid Mech.* 50:285.
24. Kolmogorov, A. N. 1941. local structure of turbulence in an incompressible fluid for very large Reynolds numbers. *Dokl. Acad. Sci. USSR* 31:301. (Reprint: Friedlander, S. K., and L. Topper, eds. 1961. *Turbulence: Classic papers on statistical theory*. N.Y.: Interscience Publs.)
25. Tennekes, H., and J. L. Lumley. 1972. *A first course of turbulence*. MIT Press.

26. Kolmogorov, A. N. 1962. A refinement of previous hypotheses concerning the local structure of turbulence in a viscous incompressible fluid at high reynolds number. *J. Fluid Mech.* 13:82.

27. Obukhov, A. M. 1962. Some specific features of atmospheric turbulence. *J. Fluid Mech.* 13:77.

28. Landau, L. D., and E. M. Lifshitz. 1959. *Fluid mechanics*. Footnote on p. 126. London: Pergamon.

29. Monin, A. S., and A. M. Yaglom. 1971. *Statistical fluid mechanics: Mechanics of turbulence*. Vol. 2. Cambridge, MA, USA: MIT Press.

30. Sreenivasan, K. R., and C. Meneveau. 1986. The fractal facets of turbulence. *J. Fluid Mech.* 173:356.

31. Frisch, U. 1995. *Turbulence: The legacy of A. N. Kolmogorov*. Cambridge – New York: Cambridge University Press.

32. Sreenivasan, K. R., and R. A. Antonia. 1997. The phenomenology of small-scale turbulence. *Ann. Rev. Fluid Mech.* 29:435.

33. Tsinober, A. 2009. *An informal conceptual introduction to turbulence*. Springer. 483.

34. Bensow, R., and C. Fureby. 2007. On the justification and extension of mixed models in LES. *J. Turb.* 8(54):1.

35. Fureby, C. 2007. On LES and DES of wall bounded flows. *Ercoftac Bulletin* 72(March).

36. Tichy, F. 1997. Laser-based measurements in non-premixed jet flames. Ph.D. Thesis. Dept. of Appl. Mech., Thermodynamics and Fluid Dynamics, Norwegian University of Science and Technology, Trondheim, Norway.

37. Magnussen, B. F. 2005. The eddy dissipation concept. *ECCOMAS Thematic Conference on Computational Combustion*. Lisbon, Portugal.

38. Drew, D. A. 1983. Mathematical modeling of two-phase flow. *Ann. Rev. Fluid Mech.* 15:261.

39. Fedina, E., and C. Fureby. 2010. A comparative study of flamelet and finite rate chemistry LES for an axisymmetric dump combustor. *J. Turb.* 12(24).

40. Weller, H. G., G. Tabor, A. D. Gosman, and C. Fureby. 1998. Application of a flame-wrinkling LES combustion model to a turbulent shear layer formed at a rearward facing step. *Proc. Combust. Inst.* 27:899.

41. Ma, T., O. Stein, L. Dorri, N. Chakraborty, and A. M. Kempf. 2010 (submitted to CNF). A-posteriori comparison of algebraic flame surface density models for LES.

42. Williams, F. A., K. Seshadri, and R. Cattolica. http://maeweb.ucsd.edu/combustion/cermech/.

43. Giacomazzi, E., F. R. Picchia, and N. Arcidiacono. 2007. On the distribution of Lewis and Schmidt numbers in turbulent flames. *30th Meeting on Combustion, Italian Section*. Ischia.

44. Vagelopoulos, C. M., and F. N. Egolfopoulos. 1998. Direct experimental determination of laminar flame speeds. *Proc. Combust. Inst.* 27:513.

45. Bossschaart, K., and L. deGoey. 2004. The laminar burning velocity of flames propagating in mixtures of hydrocarbons and air measured with the heat flux method. *Combust. Flame* 136:261.
46. Marley, S., and W. Roberts. 2005. Measurements of laminar burning velocity and Markstein number using high-speed chemiluminescence imaging. *Combust. Flame* 141:473.
47. Weller, H. G., G. Tabor, H. Jasak, and C. Fureby. 1997. A tensorial approach to CFD using object oriented techniques. *Comp. Phys.* 12:629.
48. Drikakis, D., C. Fureby, F. F. Grinstein, and M. Liefendahl. 2007. ILES with limiting algorithms. In: *Implicit large eddy simulation: Computing turbulent fluid dynamics*. Eds. F. F. Grinstein, L. Margolin, and B. Rider. Cambridge University Press. 94.
49. Van Leer, B. 1977. Towards the ultimate conservative difference scheme III. Upstream-centered finite-difference schemes for ideal compressible flow. *J. Comp. Phys.* 23:263.
50. Rhie, C. M., and W. L. Chow. 1983. Numerical study of the turbulent flow past an airfoil with trailing edge separation. *AIAA J.* 21:1525.
51. Sjunnesson, A., S. Olovsson, and B. Sjöblom. 1991. Validation rig — a tool for flame studies. Trollhättan, Sweden: VOLVO Aero AB.
52. Sjunnesson, A., C. Nelson, and E. Max. 1991. LDA measurements of velocities and turbulence in a bluff body stabilized flame. *Laser Anemometry*. 3.
53. Sjunnesson, A., P. Henriksson, and Löfström. 1992. CARS measurements and visualization of reacting flows in a bluff body stabilized flame. AIAA Paper No. 92-3650.
54. Fureby, C. 2000. Large eddy simulation of combustion instabilities in a jet-engine afterburner model. *Combust. Sci. Tech.* 161:213.
55. Baudoin, E., K. J. Nogenmyr, X. S. Bai, and C. Fureby. 2009. Comparison of LES models applied to a bluff body stabilized flame. AIAA Paper No. 2009-1178.
56. Poinsot, T. J., and S. K. Lele. 1992. Boundary conditions for direct simulation of compressible viscous reacting flows. *J. Comp. Phys.* 101:104.
57. Jeong, J., and F. Hussain. 1995. On the identification of a vortex. *J. Fluid Mech.* 285:69.
58. Rauschenbach, B. V. 1961. *Vibrational combustion*. GIFML. [In Russian.] (English Translation: 1975. Moscow: Mir.)
59. Yeung, P. K., S. B. Pope, and B. L. Sawford. 2006. Reynolds number dependence of Lagrangian statistics in large numerical simulations of isotropic turbulence. *J. Turb.* 7:1.